



# Mechanical instability tuning of a magnetorheological elastomer composite laminate

Vincent W. Chen<sup>a,b</sup>, Nitesh Arora<sup>c</sup>, Artemii Goshkoderia<sup>d</sup>, Carson L. Willey<sup>a,b</sup>, Zafer Turgut<sup>e</sup>, Philip R. Buskohl<sup>a</sup>, Stephan Rudykh<sup>c,f,\*</sup>, Abigail T. Juhl<sup>a,\*\*</sup>

<sup>a</sup> Soft Matter Branch, Materials and Manufacturing Directorate, Air Force Research Laboratory, Wright Patterson Air Force Base, USA

<sup>b</sup> UES, Inc., Dayton, USA

<sup>c</sup> Department of Mechanical Engineering, University of Wisconsin-Madison, Madison, WI, USA

<sup>d</sup> Department of Aerospace Engineering, Technion – Israel Institute of Technology, Haifa, 32000, Israel

<sup>e</sup> Air Force Research Laboratory, Wright Patterson Air Force Base, USA

<sup>f</sup> School of Mathematical and Statistical Sciences, University of Galway, Galway, Ireland

## ARTICLE INFO

Editor: Dr Uday Vaidya

## ABSTRACT

Magnetorheological elastomers (MRE) can change their shape and properties when activated by an external magnetic field. The attractive tunable properties of this stimuli-responsive composite can be further amplified by utilizing the magneto-mechanical instability phenomenon, frequently leading to dramatic microstructure transformation. In this work, we investigate the buckling behavior of the composite system consisting of a magnetoactive layer embedded into an inactive elastomeric matrix. The composite is subjected to compressive strains in the presence of a high magnetic field. Our experimental results show that the critical buckling strain is highly tunable by the applied magnetic field. In particular, the composite buckles significantly earlier when the field is applied, leading to well-developed controllable wavy patterns in the post-buckling regime. To elucidate the mechanisms associated with the experimentally observed magneto-mechanical instability, we investigated the stability using numerical analysis. The developed computational model utilizes our new experimental data on the mechanical and magnetic properties of the composite (including magnetization and the magnetic susceptibility of the MRE composite as a function of the volume fraction of magnetic particles). The numerical model is verified against the experimental results, showing its capability to predict the onset of the magneto-mechanical instability and the post-buckling behavior of the MRE. Collectively, the study demonstrates MRE instability tuning in a laminate form factor and outlines the strategy and benefits of harnessing two field physics for controlling bifurcations.

## 1. Introduction

Mechanical instabilities are pervasive in natural processes such as the closing of the Venus flytrap [1], the dispersal of plant or fungal spores [2], and the formation of fingerprints [3]. Understanding the dynamics of a system that undergoes mechanical instability, like buckling, can serve to predict and prevent failure in structural materials. However, instead of working to prevent instability formation, biomimicry of these natural systems seeks to develop functional materials that exploit mechanical instabilities for smart applications. For instance, thin conductive buckled beams are used for stretchable electronics [4],

energy absorption [5], materials with multistable features are utilized for embedded logic [6–9], and 3D-printed bi-stable structures are manufactured for actuation [10]. A summary of recent trends and advancements in buckling-induced smart materials can be found in the review by Hu and Bugueno [11].

Instability tuning with combined loading from multiple physics presents a novel opportunity to navigate the bifurcation landscape in ways that are inaccessible with only mechanical loading. Rather than solely relying on the mechanical forcing of material to achieve a meta-stable state, it can be advantageous to use an external stimulus to change the material properties to remotely trigger the instability. Adaptive

\* Corresponding author. Department of Mechanical Engineering, University of Wisconsin-Madison, Madison, WI, USA.

\*\* Corresponding author.

E-mail addresses: [rudykh@wisc.edu](mailto:rudykh@wisc.edu) (S. Rudykh), [abigail.juhl.1@us.af.mil](mailto:abigail.juhl.1@us.af.mil) (A.T. Juhl).

<https://doi.org/10.1016/j.compositesb.2022.110472>

Received 20 July 2022; Received in revised form 24 November 2022; Accepted 14 December 2022

Available online 16 December 2022

1359-8368/© 2022 Elsevier Ltd. All rights reserved.

materials such as dielectric elastomers or magnetorheological elastomers can harness electromechanical or magneto-mechanical coupling to regulate instability. For example, dielectric elastomers were included in a soft multilayered dielectric stack to determine how electrically-induced finite deformations affect their stability [12–14]. Magnetic field interactions with ordered arrays of ferrous cylinders have also been shown to induce buckling periodicities of higher order, which are inaccessible with only mechanical loads [15]. In another instance, a layer of magnetorheological elastomer was placed over a neat elastomer, and the effects of magnetic and mechanical forces on the buckling of the bilayer structure were measured [16]. This work strives to determine if buckling instability can be induced in a laminated magnetorheological elastomer via an applied magnetic field to provide a quick remotely-triggered geometric reconfiguration.

Magnetorheological elastomers (MREs) are fabricated by cross-linking micron-scale magnetic particles within an elastomeric matrix. The magnetic particles can be isotropically dispersed throughout the matrix, or a magnetic field can be applied to the sample (during polymerization) so that aligned columns of magnetic particles are formed. In either system, it has been consistently shown that the shear stiffness of an MRE increases fast and reversibly with an applied magnetic field, as reported in the double lap shear tests [17], magnetorheology [18], and dynamic mechanical analysis [19]. In addition, anisotropically loaded MREs show a stronger stiffening effect over isotropic MREs in the aligned direction [20]. In general, the storage and loss modulus of an MRE depend on the: (i) magnetic field-induced particle interactions (ii) the viscoelasticity of the matrix, and (iii) the adhesion of the particles to the matrix [21]. However, the experimental literature lacks a consensus on the effect of magnetic field on the MRE damping behavior as described by Li and Sun [22], with some articles claiming an increase, decrease, or unclear change in loss factor with an applied magnetic field. A recent comprehensive review of magneto-mechanical characterization of MREs by Bastola and Hossain [23] provides additional context on these challenges.

The complexity of the MRE response to combined mechanical and magnetic fields is exacerbated in mechanical instability studies, where small changes in stiffness, geometric, and perturbation forces influence a critical buckling event. Coupled magneto-mechanical material modeling has provided a useful lens to interpret MRE behavior [24–36], with a particular focus on instability effects in the literature. In 1968, Moon and Pao pioneered a model to determine the critical buckling point of a magnetoelastic thin plate constrained in a transversely-applied magnetic field, and their results were compared to experiments [37]. Later, in 2008, Kankanala et al. developed a continuum mechanics formulation that described the instability formation of an MRE rectangular block subjected to plane-strain deformation and a transversely applied magnetic field [38]. Ottenio et al. derived the coupled linearized (or incremental) equations superimposed on large deformations (building on the formulation by Dorfmann and Ogden [39]) to analyze the surface instabilities in a magnetoactive half-space [40]. Danas et al. determined the effect of a magnetic field on a surface layer of MRE adhered to a soft elastomer layer, and validated their work with experimental studies [16, 41, 42]. Rudykh and Bertoldi analyzed the effect of anisotropic magnetic particle formation within MREs and derived the long-wave estimates for the magneto-mechanical instabilities in magnetorheological laminates [43, 44]. Recently, Pathak et al. analytically predicted the existence of unusual microscopic modes in layered MREs under the action of a magnetic field [45]. These studies help build a foundation to understand magnetoelastic coupling in MRE materials; however, more experimental research is needed to identify magnetic tuning features for magneto-mechanical applications.

MREs have found their way into diverse applications [46], such as vibration absorbers and isolators that harness the magnetically tunable storage and loss properties of the MRE [47, 48], magnetoactive phononic materials with tunable bandgaps [49–53], or even in robotic devices that utilize global magneto-deformation of MRE samples for tactile

feedback [54]. In this study, we investigate the capacity of a magnetic field to tune the wrinkling instability in the MRE stiff/soft composite laminate, with an eye toward how this can impact practical applications. First, the study experimentally characterizes the mechanical and magnetic properties of the fabricated MRE formulation. Next, we perform the experimental investigation of the buckling development in the MRE laminate under mechanical and magnetic loading sweeps. Further, a large deformation nonlinear magneto-mechanical computational model is implemented using the experimentally derived constitutive parameters and magnetization profile. The study concludes with a tuning diagram of how to exploit the levers of mechanical loading and magnetic field to control the wrinkling response of an MRE architecture, and how this translates into increased sensitivity and utility in practical applications.

## 2. Experimental

### 2.1. Processing and fabrication of MRE specimens

To generate the neat soft elastomeric matrix, Sylgard 184 (Ellsworth Adhesives, Germantown, WI) base and catalyst were mixed rigorously with a handheld mixer for 5 min, followed by vacuum degassing for 1 h at room temperature. The base-to-catalyst ratio was varied from 10:1 to 30:1 to tune the crosslink density and stiffness of the elastomer. The degassed mixture was poured into 3D printed molds (Flashforge Creator Pro, ABS filament) with dimensions of 20 mm × 7 mm × 7 mm and cured at 60 °C for 2 hours.

To fabricate the magnetoelastomer composite, iron powder with a 3 μm average diameter (US Research Nanomaterials Inc., Houston, TX, US) was mixed into the Sylgard 184 at volume fractions from 0 to 0.52. Iron particles were dispersed in the Sylgard 184 base prior to the addition of the catalyst. A planetary mixer (Thinky, ARE-310) rotating at 1000 RPM for 2 min produced a homogeneous mixture without causing a significant rise in temperature (<5 °C), which may lead to premature curing. The mixture was placed under a vacuum for 1 hour to remove air pockets introduced by the mixing. The iron-loaded composite was molded by casting between two acrylic sheets (McMaster Carr, Aurora, OH) with acrylic spacers (Astra Products, Copiague, NY) ranging from 0.2 to 0.5 mm thick cut by a CO<sub>2</sub> laser (Full Spectrum Laser, PS48–150W). The layer was cured at 60 °C for 2 hours. After curing, the specimen was laser cut to rectangles of 28 × 7 mm<sup>2</sup> using a 1064 nm laser cutter (Keyence, MD-X1520).

The laminate specimen was formed by layering rectangles of neat elastomer (30:1 base-to-catalyst ratio, 20 mm × 7 mm) followed by magnetoelastomer (28 mm × 7 mm), and then another layer of neat elastomer (20 mm × 7 mm). A thin layer (<100 μm) of the pre-polymerized 30:1 Sylgard 184 was applied between the layers as a chemically compatible adhesive. The assembly was secured in a 3D printed mold during 2 h of curing at 60 °C, followed by 2 hours of curing at 100 °C. A representative laminate sample can be seen in Fig. 1C.

### 2.2. Magnetic and mechanical characterization

**Magneto-Vibrometry Measurements:** To determine the magnetic properties of the magnetoelastomer, cylindrical specimens (3 mm in diameter and height) at various iron loadings were cast into acrylic molds. The samples were placed in a vibratory sample magnetometer (Lakeshore, 735 VSM) coupled to the electromagnet (GMW, 3474-140). The electromagnet was used to magnetize the MRE specimens, while simultaneously being oscillated on a mechanical shaker, and the oscillating magnetic flux from the magnetized MRE was detected by a set of pickup coils, allowing for the measurement of the magnetic moment and the saturation magnetization at various iron loading of the MRE.

**Mechanical Analysis under Quasi-static Loading.** Young's modulus of the specimen was estimated using a dynamic mechanical analyzer (TA Instruments, RSA3). Cylindrical specimens of the MRE were cast and

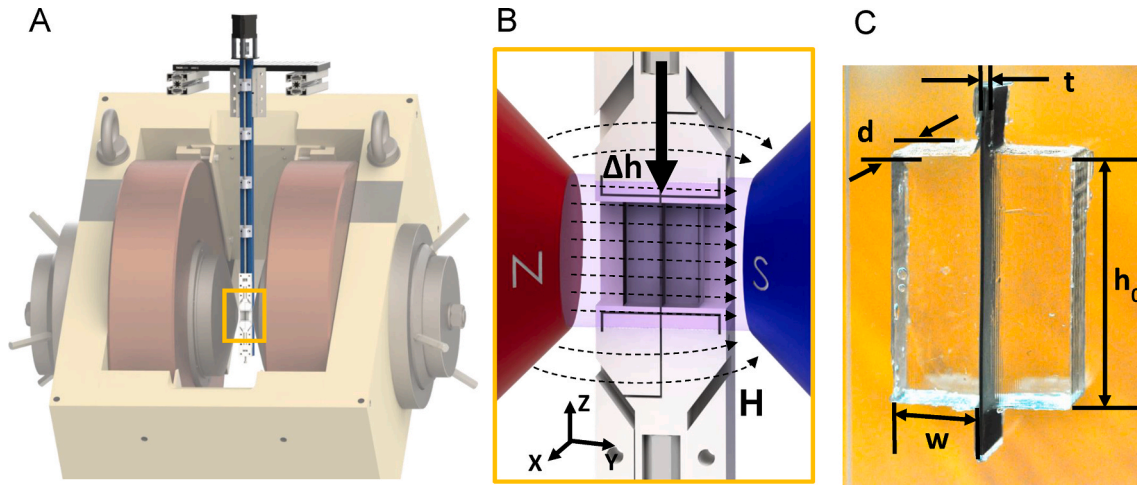


**Fig. 1.** Experimental setup of combined axial compression under transverse magnetic field. **A)** Image of MRE laminate buckling setup and the GWM 3474-140 electromagnet coils with a custom servo-driven mechanical compression stage. **B)** Image of MRE specimen in the compression stage with applied displacement ( $z$  axis) and magnetic field ( $y$  axis) orientations annotated. Highlighted region indicates the uniform magnetic field zone. **C)** Representative image of MRE laminate specimen with annotated dimensions. The MRE layer extends outside of the specimen to provide a tab for clamping in the compression grips.  $h_0 = 20$  mm,  $d = 7$  mm,  $w = 7$  mm,  $t = 0.2\text{--}0.5$  mm.

cured in PTFE molds of 6.35 mm in diameter and 6.35 mm in height. A 15% compression strain was applied to the specimen at a rate of 0.02 mm/s. Young's moduli were extracted from the slope of the stress-strain curve from the loading cycle between 2 and 10% strain.

### 2.3. MRE laminate test setup and image processing

Fig. 1A shows the experimental setup that allows simultaneous axial compression and a transverse magnetic field to be applied to an MRE laminate. The electromagnet coils can generate a uniform 2T magnetic field in the volume occupied by the laminated MRE sample. A non-magnetic compression stage was 3D printed (Fig. 1B), allowing for a plunger (activated by a servo-motor) to compress the laminate architecture while under an applied magnetic field (see Fig. S1 in the supplementary information (SI) for details). The laminate sample is constrained within the compression stage by an acrylic plate with silicone oil applied between the sample and the acrylic plate to allow for a slip at the interface. The MRE laminate long axis is oriented along the vertical mechanical loading direction ( $z$ -axis), and the magnetic field is applied horizontally ( $y$ -axis) across the laminated layers. A representative image of the MRE laminate specimen, with dimensions annotated, is shown in Fig. 1C. All specimens had a nominal initial height ( $h_0$ ) of 20 mm, a depth ( $d$ ) of 7 mm, and a width ( $w$ ) of 7 mm. The MRE layer consisted of an iron particle loading of  $\varphi = 0.29$  and included 10 distinct MRE layer thicknesses, ranging from  $t = 250\text{--}618$   $\mu\text{m}$ . The MRE layer extends beyond the non-active layers (28 mm vs. 20 mm) to enable clamping<sup>1</sup> by the compression stage, which reduces the twisting of the MRE layer under an applied magnetic field. The shared siloxane base chemistry between the neat and MRE-loaded layers resulted in a strong bonding. Attempts to pull the layers apart resulted in tearing in the soft/neat layer only. No delamination was observed upon repeated loading and unloading of the sample ( $>10$  cycles) in the compression jig.

Compression and image capture with a digital camera (Nikon, D750) were synchronized with an Arduino UNO. Systematic compression of 50  $\mu\text{m}$ /step was applied to the specimen from the resting state. The camera was set at a safe distance from the electromagnet, and a 100 mm macro lens (Tokina, AT-X PRO Macro 100) in conjunction with a  $2 \times$

teleconverter (Nikon, TC-201) were used to capture digital images. The onset of wrinkling is difficult to visually detect in experimental systems. To mitigate inconsistency in visual detection, an image processing workflow was developed to improve and standardize the detection of wrinkling across specimens. Image captures of the MRE laminate under varying degrees of compression were collected (24.3  $\mu\text{m}$ /pixel). Thresholding was applied to convert the colorized images into binary data tables, where positive pixels correspond to the MRE layer, and negative pixels correspond to the neat/soft matrix. The effective width of the MRE layer was determined by the number of columns exhibiting positive pixels. Registration marks embedded in the plungers were used to measure the height of the specimen under compression to determine the compressive strain. A critical buckling point ( $\lambda_c$ ) was defined as the intersection between two linear fits of the data prior to buckling (low slope) and after buckling (rapid rise in width). A built-in fitting function (Piecewise PWL2) in OriginPro was used to process the data. Further details can be found in the Supplementary material (Fig. S2).

## 3. Results and discussion

### 3.1. Characterization of MRE magnetic and mechanical properties

The MRE formulation and mixing protocol in this study was selected to produce an isotropic magneto-responsive material with a homogeneously dispersed mixture of spherical iron particles. The amount of iron particle loading controls the magnetization capacity of the MRE, as well as the overall stiffness, as the rigid fillers increase the mechanical properties of the MRE. To characterize this dependence, the magnetization ( $M$  [A/m]), magnetic susceptibility ( $\chi$  [—/—]), and Young's Modulus ( $E$  [MPa]) of the MRE composite were measured as a function of increasing iron volume fraction loadings (see Fig. 2). The volume fraction,  $\varphi$ , of the iron particles in the MRE is defined as,

$$\varphi = \frac{m_{Fe}/\rho_{Fe}}{m_{Fe}/\rho_{Fe} + m_{PDMS}/\rho_{PDMS}} \quad (1)$$

where  $m_x$  and  $\rho_x$  correspond to the mass and density, respectively of the iron carbonyl particles (Fe) and the neat 10:1 base:catalyst Sylgard 184 (PDMS). The densities for the iron carbonyl particles and the neat silicone were taken as 7.87 g/cm<sup>3</sup> and 1.05 g/cm<sup>3</sup>, respectively.

Using magneto-vibrometry, the magnetization and susceptibility of the MRE composite were collected at various iron volume fractions and

<sup>1</sup> We have verified through simulations that the clamping of MRE layer does not influence the instability development in laminates.

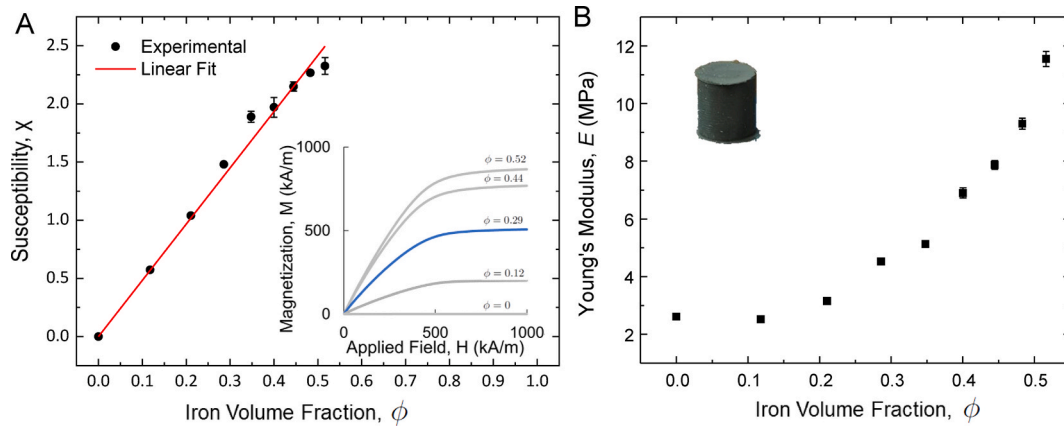


**Fig. 2. MRE Characterization: Effect of Iron Loading** A) Increase in magnetic susceptibility with Fe loading. Vibrating magnetometer susceptibility data as a function of Fe particle volume fraction. mean  $\pm$  stdev,  $n = 3$ . **Inset:** Magnetization vs applied field curves highlight saturation at  $\sim 550$  kA/m ( $B = \sim 0.7$  T). B) Young's modulus of homogenous MRE specimens under uniaxial compression ( $\lambda_{max} = 0.75$ ), mean  $\pm$  stdev for number of specimens,  $n = 3$ . Base-to-catalyst ratio is 10:1. **Inset:** Example specimen with the cylindrical shape (diameter,  $d = 6.36$  and height,  $h = 6.35$  mm) used for dynamic mechanical analysis.

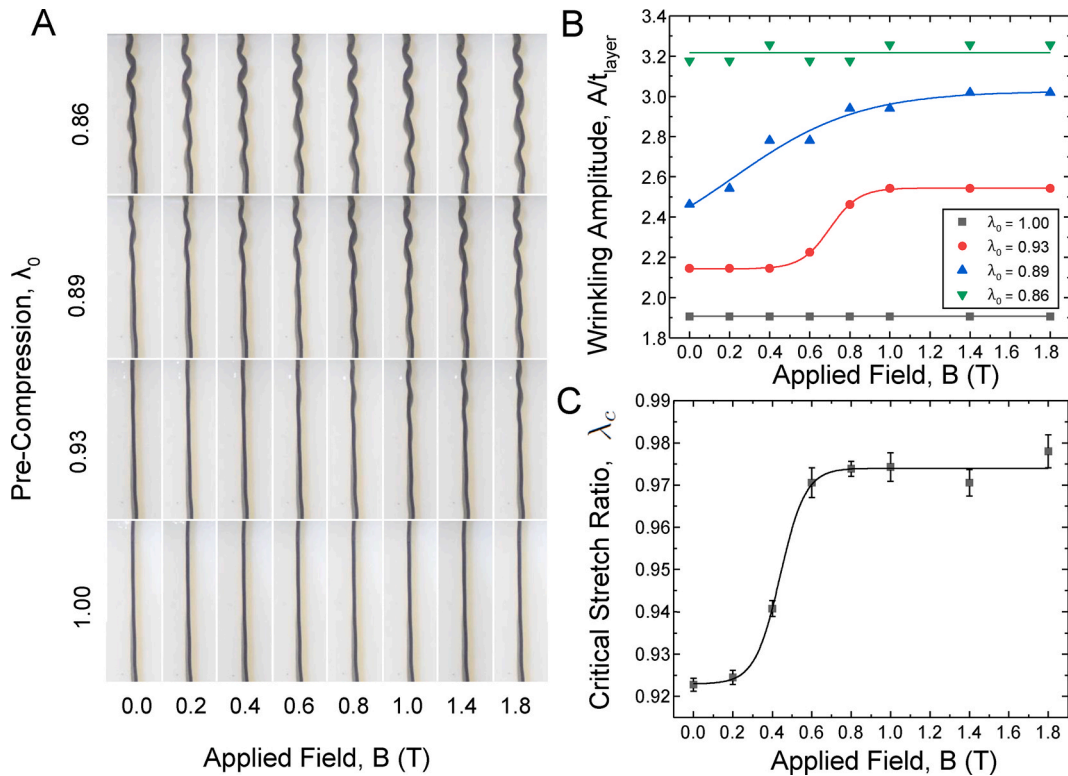


**Fig. 3. Magnetic field triggers wrinkling instability.** Experimental results of specimen under combined axial compression and transverse magnetic field. A) Image array of single layer MRE under fixed pre-compression and increasing applied field. Width of each image is 4.8 mm ( $\varphi = 0.29$ ,  $t = 306 \pm 2.4$   $\mu$ m). B) Plot of average amplitude of wrinkled MRE layer as function of pre-compression and applied magnetic field. Note: no significant change in amplitude observed in  $\lambda_0 = 1.00$  (pre-buckled) and  $\lambda_0 = 0.86$  cases (post-buckled). C) Critical stretch ratio determined from strain sweep experiments at fixed B-fields.

are presented in Fig. 2A. Magnetization, defined as the density of induced magnetic dipoles, is plotted vs. the applied magnetic field,  $H$ , in the inset. No magnetization is detected when the iron particles are not added to the matrix ( $\varphi = 0$ ), demonstrating that the neat elastomer is insensitive to the magnetic field. Magnetization increases significantly with increasing volume fraction of iron, reaching a maximum magnetization strength of 837 kA/m for the highest iron loading of  $\varphi = 0.52$ . The magnetization curves consistently saturate at an applied magnetic

field of approximately 550 kA/m ( $B = 0.7$  T) across all loadings. The magnetic susceptibility,  $\chi$ , in this study is taken as the maximum slope of the magnetization vs applied magnetic field curve. The magnetic susceptibility increased linearly within the range of volume fractions investigated with a slope of 4.8 (R-square = 0.997), which is in line with values reported in the literature ( $\chi = 2.5 - 5.0$  for 3–6  $\mu$ m particles [27]). Negligible remnant magnetization was observed in the MRE specimens, which is consistent with the soft magnet nature of the iron



particles (see SI section S2 for fitting details).

The effect of iron particle loading and base: catalyst ratio on the mechanical properties of the MRE composite was also characterized. Compression-based estimates of Young's modulus,  $E$ , for the MRE composite as a function of the iron volume fraction is depicted in Fig. 2B. Based on quasi-static compression testing a DMA, the 10:1 base to catalyst ratio for the PDMS matrix resulted in Young's modulus of  $E = 2.61$  MPa without iron fillers ( $\varphi = 0$ ). With increasing iron filler volume fraction, the stiffness of the MRE composite increased to  $E = 11.5$  MPa at  $\varphi = 0.52$ , a 4.4x increase in stiffness from the matrix alone. The base: catalyst ratios of 20:1 and 30:1 were also tested, yielding Young's Moduli of  $882 \pm 50$  kPa and  $267 \pm 43$  kPa (mean  $\pm$  stdev,  $n = 10$ ), respectively (see Fig. S4). The compression stiffness of the 10:1 ratio is approximately 8.75x greater than the 30:1 ratio. Silicone oil was also added as a plasticizer to further reduce the stiffness of the matrix, reaching Young's Moduli as low as  $27 \pm 4$  kPa (mean  $\pm$  stdev,  $n = 10$ , see Fig. S4). However, the silicone oil infiltrated and swelled the pre-formed MRE composite layer and was not used for the laminate buckling tests. A brief description of the alternative matrix formulations and a summary of their mechanical properties is included in the SI.

### 3.2. Characterization of critical stretch ratio tuning

The magnetic response and tunable mechanical properties of MREs are ideal material behaviors to leverage for multi-field control of buckling instabilities in composite architectures. Building off prior work on magnet-driven wrinkling in thin films on an elastic substrate [42] and the deflection of an MRE membrane subjected to a non-uniform magnetic field [55], a finite-sized laminate design was selected for this study to highlight the tuning capacity of the critical wrinkling strain under orthogonally applied magnetic field. Fig. 3A displays images of this experimental wrinkling behavior of a single MRE laminate specimen (MRE layer,  $\varphi = 0.29$ ,  $t = 306 \pm 2.4$   $\mu\text{m}$ ) under various states of pre-compression ( $\lambda_0$ ) at continually increasing applied magnetic fields. The stiffness ratio of the laminate with  $\varphi = 0.29$  particle loading, and no applied field, was  $E_l/E_m = 15.97$  ( $E_l$  – Young's modulus of the MRE layer  $4.76 \pm 0.35$  MPa vs.  $E_l$  – Young's modulus of the elastomeric matrix  $298 \pm 16$  kPa) based on the compression measurements of the previous section. Without any applied magnetic field, Fig. 3A shows that the laminate geometry has not wrinkled at a pre-compression of  $\lambda_0 = 1.00$  or  $\lambda_0 = 0.93$ . However, at a pre-compression of  $\lambda_0 = 0.89$ , the onset of wrinkling in the laminate has already begun, and it is detectably wrinkled at  $\lambda_0 = 0.86$ . While  $\lambda_0 = 0.93$  showed no wrinkling when the field

was off, the onset of wrinkling was observed when the field was raised to 0.6 T. The amplitude of wrinkling appears to quickly plateau as the field exceeds the saturation strength of 0.7 T. Higher compression ( $\lambda_0 = 0.89$ ) resulted in wrinkling without the aid of magnetic stiffening, as indicated by  $\lambda_c > 0.92$  in Fig. 3C but applied magnetic field did increase the amplitude of the wrinkled MRE layer.

Strain-sweep experiments were performed with fixed applied magnetic fields of 0.2, 0.4, 0.6, 0.8, 1.0, 1.4, and 1.8 T. The critical stretch ratio of each strain-sweep experiment is plotted against the applied magnetic field in Fig. 3C, and it indicates that without any magnetic field, the sample will begin to wrinkle around  $\lambda = 0.92$ . Low applied fields ( $< 0.2$  T) resulted in minimal change to  $\lambda_c$ . A modest level of the applied field (0.6 T) reduced the compression necessary to achieve wrinkling from  $\lambda_c = 0.92$  to 0.97. Past 0.7T, the critical wrinkling point appears to plateau at  $\lambda_c = 0.97$ , which correlates with the saturation field strength of the magnetization curves in Fig. 2A. Saturation may also be a factor in the applied field sweep of Fig. 3B, as indicated by the plateau in wrinkling amplitude above 0.6–0.7 T for the pre-compression states of  $\lambda_0 = 0.89$  and  $\lambda_0 = 0.93$ . Similar trends in the wrinkling behavior with applied magnetic field were observed across all of the MRE layer thicknesses ( $t_{nom} = 258$ –598  $\mu\text{m}$ ,  $n = 10$ ) investigated at this iron particle loading ( $\varphi = 0.29$ ) for the laminate specimens (see Figs. S5 and S6 for representative low and high thickness examples).

Combining the critical stretch ratio results across all laminate specimens, two dominant features of magnetic tuning are observed. First, the MRE laminate consistently wrinkles at lower strains when the magnetic field is applied (1.8T) compared to only mechanical loading (0T). As shown in Fig. 4A, an applied magnetic field produced a marked increase in the critical stretch ratio for all MRE layer thicknesses investigated. The average change in stretch critical ratio was  $\Delta\lambda_c = 0.045 \pm 0.012$  between 0 and 1.8 T, which is effectively a 5% change in the critical stretch ratio. While a seemingly small value, this 5% shift is more than sufficient to reversibly trigger the wrinkling instability by cycling on and off the magnetic field at modest pre-compressions. Shifts in the critical stretch ratio in the range of 0.04–0.05 were observed at the lower, post-saturation applied field of 0.8T, indicating that reversible buckling could be leveraged at more modest magnetic fields (see Table S1 for full data set of critical stretch ratio vs. applied magnetic field). The wrinkling behavior of stiff/soft laminates with a single thin stiff layer was previously analyzed by Li et al. [56] for the mechanical loading only scenario. The study showed that the critical strain,  $\epsilon_c$ , for wrinkling scales with the stiffness ratio of stiff/soft layers by  $(E_l/E_m)^{-2/3}$ , according to the following specific closed form solution for plane strain loading:

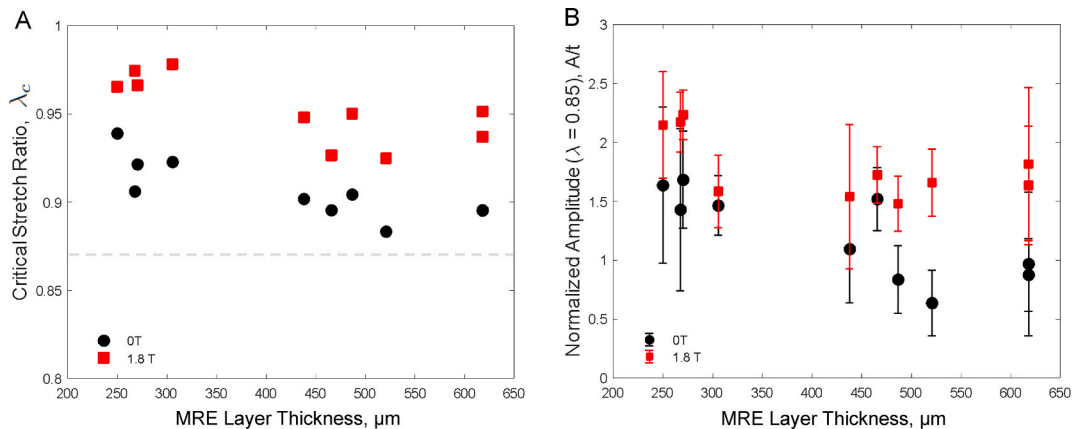


**Fig. 4.** Magnetic field regulates critical stretch ratio and post-buckling amplitude. **A)** Critical stretch ratio of laminate interface wrinkling with (1.8T) and without (0T) applied magnetic field across laminate specimens with different MRE layer thicknesses. Thickness was measured at multiple points along the length the MRE layer and averaged. Dashed line denotes theoretical critical stretch ratio ( $\lambda_c = 0.87$ ) based  $\varphi = 0.29$  laminate stiffness ratio,  $E_l/E_m = 16$  [10]. **B)** Amplitude of wrinkle instability normalized by the MRE layer thickness with and without magnetic field. Amplitude measurements were collected at a stretch ratio of  $\lambda = 0.85$  and tabulated as mean  $\pm$  stdev of the amplitudes across all wrinkles in the specimen ( $n = 4$ –9).

$$\varepsilon_c = 3^{2/3} \left[ \frac{3 - 4\nu_m}{(1 - \nu_m)^2} \right]^{-2/3} \left( \frac{E_l}{E_m} \right)^{-2/3} \quad (2)$$

where  $\nu_m$  is the Poisson's ratio of the soft matrix layers. Assuming incompressibility ( $\nu_m = 0.5$ ), the critical compression strain for the laminate stiffness ratio of  $E_l/E_m = 16$  equals  $\varepsilon_c = 0.13$ . Using the deformation gradient for uniaxial, plane strain compression ( $\mathbf{F} = \text{diag}(1, 1/\lambda, \lambda)$ ) and the Green-Lagrange strain tensor, the critical stretch ratio predicted by linear analysis in Li et al. [56] is  $\lambda_c^{(Li)} = 1 - \varepsilon_c = 0.87$ . The theoretical estimate is plotted as the dashed gray line in Fig. 4A for reference. The analytical expression for the critical stretch ratio was also fit to the experimental data to estimate the stiffness ratio of best fit. Minimizing the sum of squared errors between the model and experiment for all laminate specimens, the estimated stiffness ratios were  $E_l^{fit}/E_m = 28.2$  and  $74.3$  for the 0 T and 1.8 T data sets, respectively ( $\lambda_c^{fit} = 0.91$  at 0T and  $\lambda_c^{fit} = 0.95$  at 1.8T). If the shift in the critical stretch ratio was strictly driven by the stiffness ratio, this analysis would suggest the magnetic field increases the stiffness of the MRE layer by  $\sim 2.6\times$ . However, as seen in the next section, the wrinkling wavelength (which should also scale with the stiffness ratio) showed no statistical difference between the 0T and 1.8T applied magnetic fields. This suggests that there is an alternative tuning mechanism is also at play, in addition to the stiffness ratio modification induced by the magnetic field.

We notice that in the experiments all the specimens under no magnetic field develop instability before the theoretical prediction of  $\lambda_c^{(Li)} = 0.87$ . One of the reason behind this discrepancy is that the analysis employed to obtain this critical strain value assumes the linear elastic response of stiff layer and the soft matrix. It does not account for the non-linear regime of large deformations. As we will see in the next section, where the non-linear hyperelastic model is employed to define the behavior of phases, in simulations, the deformation required to trigger wrinkling is smaller than the theoretical prediction. Additionally, the discrepancy can be induced due to the manufacturing imperfections, loading perturbations, or highly non-linear behavior of phases (for example, strain-stiffening and viscoelasticity), which are not considered in the present model. Interestingly, both the 0T and 1.8T critical stretch ratio data plots exhibit a small, negative linear correlation with increasing thickness (Fig. 4A). This slight dependence on thickness may indicate that the laminate specimens with higher thickness are less sensitive to these imperfections, as the relative size of the defects to the MRE layer thickness decreases.

### 3.3. Characterization of post-wrinkling amplitude tuning

The second dominant feature of magnetic tuning is the increase in the amplitude of the post-wrinkling pattern with applied magnetic field. Dynamic tuning of the wrinkling amplitude is of interest as it could have utility for precisely aligning and shaping the internal structure of the MRE instability pattern. The amplitude and wavelength of the post-wrinkled patterns were collected at an applied compression of  $\lambda = 0.85$  with, and without, an applied magnetic field. As seen in Fig. 4B, the amplitude of the wrinkling pattern increased with the magnet active, exhibiting a normalized mean increase of  $A/t = 0.58 \pm 0.28$  (mean  $\pm$  stdev) across all 10 specimens of varying thickness. The error bars in Fig. 4B denote the standard deviation of amplitudes across all peaks in the wrinkled MRE layer, which range from 9 peaks for the thinner MRE layers to 4 peaks for the thicker. Similar to the critical stretch ratio feature, the magnetic-driven increase in wrinkling amplitude was also reversible. No statistically significant change in wavelength,  $L$ , was observed between 0T and 1.8T applied field (see Fig. S7). Again, referencing the linear analysis of Li et al. [56], the wavelength of wrinkling in the mechanics-only case scales as  $L \propto (E_l/E_m)^{1/3}$ . Fitting the wavelength vs. thickness data using the plane strain-based analytical model [56], the stiffness ratio for both the 0T and the 1.8T magnetic field had

comparable values ( $E_l/E_m = 25.6$  at 0T and  $26.7$  at 1.8T). This result suggests that mechanical stiffening of the MRE layer under the applied field is not the primary tuning mechanism of elastic instability.

Laminate specimens with higher iron loadings in the MRE layer ( $\varphi = 0.44$  and  $0.52$ ) were also prepared. The stiffness ratio between the MRE layer and the neat elastomer at these iron loadings of  $\varphi = 0.44$  and  $0.52$  were  $E_l/E_m = 29.5$  and  $43.2$ , respectively. However, these MRE layers reacted strongly to the magnetic field and induced twist deformations that were incompatible with the plane strain assumption of our laminate wrinkling analysis. Under modest field intensities (0.4–0.6 T) and no pre-compression ( $\lambda_0 = 1.0$ ), these MRE layers experienced attraction to one of the magnet poles, bending the MRE layer from the center (see Fig. S9). Similar behavior was observed even at higher pre-compressions. This simple bending mode has a much longer wavelength than the harmonic wrinkling displacement field for a stiff/soft laminate interface, creating a perturbation that is incompatible with interface wrinkling. In addition, further increase in the magnetic field resulted in the MRE twisting along the z-axis in an attempt to align the depth of the MRE with the magnetic field lines (see Fig. S9 for representative images). Magnetic field perturbations, finite-size effects, and out-of-plane deformations of this nature highlight some of the challenges of experimental validation of magneto-mechanical phenomena, as the relative contributions of mechanical and magnetic energy should be balanced for the system to be effectively coupled and not be dominated by either physics.

### 3.4. Computational analysis of magneto-mechanical instabilities

Next, we numerically study the post-buckling behavior of the MRE laminate. We employ an amended energy potential to define the constitutive behavior of each phase consisting of the elastic and magnetic parts [27]. In particular, an augmented neo-Hookean nonlinear material model is used (see SI for more details). Following the experiments, the soft matrix is modeled with an initial shear modulus  $G_m = 100\text{kPa}$  ( $E_m \approx 300\text{kPa}$  and  $\nu_m \approx 0.5$ ), and the stiffness ratio between the MRE layer and matrix is  $G_l/G_m = 16$ . The matrix is considered to be magnetically inactive, while the magnetic response of the MRE layer is modeled according to the relation between the induced magnetization

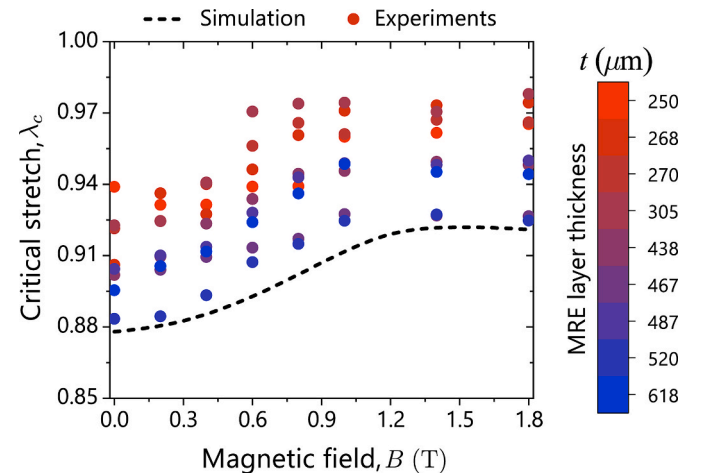
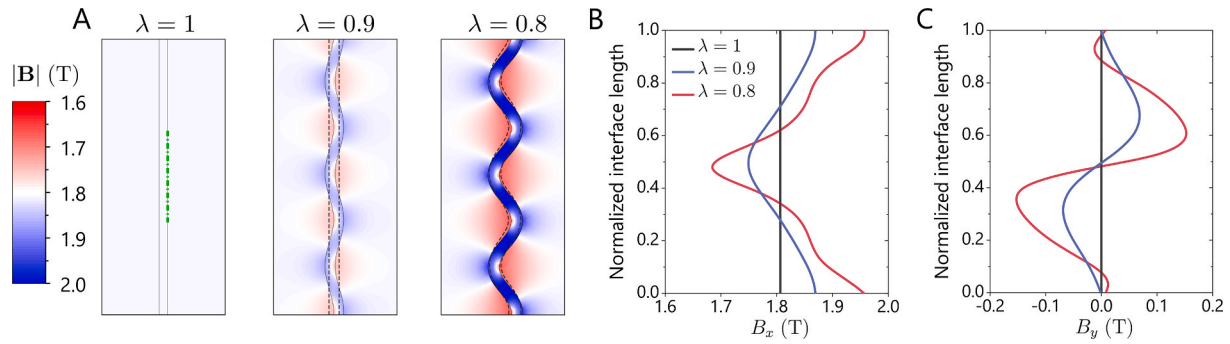


Fig. 5. Computational model captures trend in magnetic tuning of critical stretch ratio. Plot of critical stretch ratio vs magnetic field strength with experimental data (dots) and simulation prediction (dashed curve). Experimental data is color coded by the nominal MRE layer thickness of each specimen ( $n = 10$ ). In the simulations, a periodic RVE of the composite with 1% volume fraction of MRE layer is considered. Note: thicker MRE specimens (blue) most closely match the predicted instability curve, while thinner MRE layers (red) wrinkle earlier. (For interpretation of the references to color in this figure legend, the reader is referred to the Web version of this article.)



**Fig. 6.** Magnetic field amplifies wrinkling amplitude with geometry-induced local field distribution. **A)** Color plot of magnetic field intensity at an applied field of 1.8 T with applied stretch ratios of  $\lambda = 1, 0.9$  and  $0.8$ . Black dashed line denotes the deformation configuration of the MRE layer without magnetic field applied (0 T). Plots of the local magnetic field, separated into **B)** aligned ( $B_x$ ) and **C)** orthogonal ( $B_y$ ) directions to the applied field, evaluated along the MRE layer/soft matrix interface at the undeformed, pre-wrinkling and post-wrinkling stretch ratios. The dotted green line in panel A denotes the single wavelength of the interface length plotted in panels B and C. (For interpretation of the references to color in this figure legend, the reader is referred to the Web version of this article.)

and the applied magnetic field observed experimentally (see Fig. S10). In simulations, we consider a periodic representative volume element (RVE) of the composite with height  $L$  and width  $a$ , and thickness of MRE layer  $t$  (see Fig. S11). The RVE is subjected to in-plane magneto-mechanical loading with compression along the  $e_2$ -direction and magnetic field along the  $e_1$ -direction. In the simulations, the loading condition is implemented by applying periodic boundary conditions for both the displacement and magnetic field [44]. To implement the single-layer setup (as in experiments), we consider the laminate with a very small volume fraction of MRE layer, i.e.,  $c_l = 0.01$ , hence,  $t = 0.01a$ . The details of the post-buckling analysis performed to evaluate the critical parameters corresponding to the onset of instability are provided in Supplementary subsection S8.2.

The model was first utilized to investigate the role of the magnetic field in tuning the critical stretch ratio for MRE wrinkling. The experimental data ( $n = 10$ ) and the computationally predicted critical stretch ratio vs magnetic field curves are plotted in Fig. 5. The computational model captures the qualitative trend of the experimental data, exhibiting the initial reduction and then plateau in the critical stretch with increasing field strength. However, the model predicted quantitatively higher critical deformation levels for all values of the applied field. This is largely due to the experiment fabrication and testing variability issues, which lead to the premature triggering of the wrinkling instability. As

discussed in the previous section, the thinner MRE layer specimens exhibit earlier wrinkling initiations than the thicker MRE layers. The trend in thinner MRE layers wrinkling at lower stretch ratio is clearly seen in the color coding (red – thinner, blue – thicker) of the data in Fig. 5. We found that the trend observed here in the experiments can be attributed to the geometric imperfections. In particular, we observed that the wrinkling detection method used on the experimental data (see Supplementary Information Sec. S2) has higher sensitivity to the imperfections in thinner MRE layers. Interestingly in the mechanical-only case (0 T), the hyperelastic material model predicted a slightly higher critical stretch ratio ( $\lambda_c = 0.878$ ) than the linear elastic model ( $\lambda_c = 0.87$  [56]). Although small, this difference highlights the influence of the choice of a constitutive model for the wrinkling mechanics simulation. Furthermore, we note that although the MRE layer is modeled as a homogenized continuum material, it is a composite with iron particles embedded in a soft matrix. Therefore, it may exhibit highly non-linear mechanical behavior (for example, strain stiffening), which are not accounted for in the present study. These material behavior uncertainties can induce additional discrepancies and require full multi-scale modeling to be resolved.

The computational model was next utilized to investigate the local magnetic field distribution within the MRE laminate composite as a function of mechanical compression. Color plots of the magnetic field

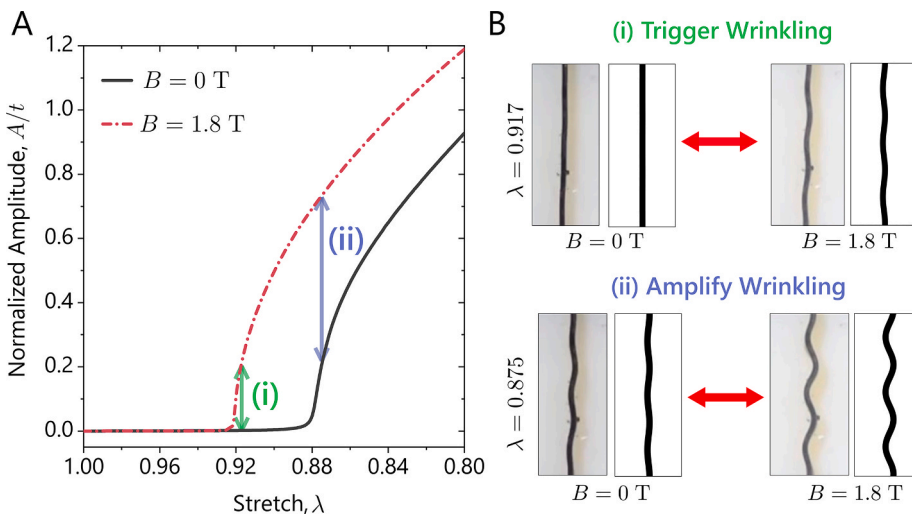


**Fig. 7.** Leveraging Magnetic Field to Control Wrinkling Behavior. **A)** Plot of modeling predictions of normalized wrinkling amplitude,  $A/t$ , vs stretch ratio,  $\lambda$ , with and without applied magnetic field. Magnetic tuning features include (1) triggering wrinkling at lower compressions, (2) amplifying the amplitude of the wrinkling pattern in post-buckling, and (3) maintaining the wrinkling amplitude under varying compression by simultaneous adjusting the magnetic field. **B)** Representative example of (1) triggering wrinkling with magnetic field (1.8 T) at a pre-buckling stretch ratio ( $\lambda_0 = 0.917$ ) and (2) amplifying wrinkling amplitude at post-buckling stretch ratio ( $\lambda_0 = 0.875$ ). MRE layer thickness,  $t = 466 \pm 27 \mu\text{m}$ .



intensity,  $|\mathbf{B}| = \sqrt{B_x^2 + B_y^2}$ , are shown in Fig. 6A under an applied magnetic field of  $B = 1.8\text{ T}$  for mechanically-applied stretch ratios of  $\lambda = 1, 0.9$ , and  $0.8$ . In the reference configuration, the magnetic field intensity is uniform and equal to the applied field of  $1.8\text{ T}$ . However, as wrinkling initiates in the MRE layer, the magnetic field starts to vary along the length of the MRE layer due to the perturbed wrinkling geometry. The magnitude of this field variation increases as more mechanical compression is applied, reaching approximately a 10% deviation from the applied field intensity of  $1.8\text{ T}$  at  $\lambda = 0.8$ . Further focusing on this variation, Fig. 6B and C shows the local magnetic field along the interface between the MRE layer and soft matrix, separated into directions aligned ( $B_x$ ) and orthogonal ( $B_y$ ) to the applied field. Fig. 6B and C zoom in on a single wavelength of the MRE layer, where the wavelength location is denoted by the green dash-dotted line in Fig. 6A. The magnetic field intensity increases at the peaks of the wrinkled MRE interface, but it decreases at the troughs in the wrinkled MRE interface. At small wrinkling amplitudes (modest applied stretch ratios), the magnetic field at the MRE layer interface nearly follows the profile of the wrinkling displacement. However, at larger wrinkling amplitudes, the magnetic field in the  $x$ -direction becomes even more intensely localized to the crest and peak points along the MRE interface, and the profile does not follow a single frequency sine wave. For  $B_y$ , the magnetic intensity is zero at the crest and peaks of the wrinkled MRE interface, as the surface normal of the MRE layer is aligned with the field at these points. Away from these points, the vertical component,  $B_y$ , of the magnetic field cycles between positive and negative values according to the orientation of the surface relative to the applied magnetic field. This component is relatively small compared to the magnitude of the applied field ( $\sim 0.2\text{ T}$  vs.  $1.8\text{ T}$ ). However, the introduction of these attractive field variations in the vertical direction likely promotes increased wrinkling amplitudes in the post-wrinkling regime. To highlight the amplitude increase caused by the magnetic field, the deformed configuration of the MRE layer under mechanical loading only (0T) has been included as a dashed outline in the color plots of Fig. 6A. Psarra et al. [41] made a similar observation in their MRE surface layer study, suggesting that alternating attractive fields develop across the wrinkled MRE surface due to the wavy geometry. At a minimum, the localized magnetic field correlates with the early initiation of wrinkling instability and the increase in wrinkling amplitude. While other mechanisms could also be contributing to this tuning capability, such as magnetostriction and induced stiffening effects, these seem less dominant than the interaction of wrinkle geometry and the magnetic field.

A key contribution of this work was the experimental validation of two magnetic field tuning mechanism in the MRE laminate, specifically the ability to trigger wrinkling and the ability to amplify the amplitude of wrinkling in the post-wrinkling regime. We highlight these two tuning features in Fig. 7A, using a plot of normalized wrinkling amplitude ( $A/t$ ) vs. stretch ratio for an “active” ( $1.8\text{ T}$ ) and “inactive” ( $0\text{ T}$ ) magnetic field scenario. This diagram serves as a practical design guide on how much to pre-compress the laminate in order to maximize the amplitude increase induced by the magnetic field. A representative example of (i) triggering wrinkling and (ii) amplifying the wrinkle amplitude are shown in Fig. 7B, with side-by-side experimental and simulation comparisons. To highlight the reversibility, time-lapse video of the laminate wrinkling under fixed pre-compression and increasing magnetic field were compiled (see SI for the videos). The speed of triggering the wrinkling is dependent on the activation speed of the magnet. In this study, the magnet field strength was slowly incremented in order to access the effects of a quasi-static field. However, for a dynamic tuning operation, the magnet could be programmed to step more rapidly and in fewer increments between target field strengths.

#### 4. Conclusion

MREs comprised of various iron particle loadings in PDMS silicone

matrix were investigated for their use in the magnetic field-induced tuning of mechanical instabilities. The highly tailorable silicone matrix was leveraged to fabricate both the magneto-active and the soft magneto-inactive layers for the laminate specimen, with the shared base chemistry providing good interfacial compatibility. Compressive strain under varying levels of the magnetic field were applied to investigate the critical buckling strain required to trigger the wrinkle pattern formation. The critical wrinkling strain predicted by the computational model follows the trend of the experimental data, but with slightly higher quantitative estimates for the wrinkling strain. Interestingly, specimens with thicker MRE interlayers more closely match the computational predictions, suggesting that these specimens were less sensitive to artifacts from the fabrication process in triggering the early onset of buckling. The role of the magnetic field on post-wrinkling behavior is also investigated, revealing a significant increase in the amplitude of the MRE wrinkled wave profile. Moreover, in addition to the magnitude, the instability characteristics are also dictated by the direction of the applied magnetic field. In particular, we found that when the field is applied parallel to the MRE layer, it has a stabilizing effect. This is in contrast with the case when the magnetic field is applied in the perpendicular direction (see Sec. S9 in Supplementary Information).

The balance between the magnetic and mechanical loading can be tuned to provide a variety of possible designs leading to significant geometric re-arrangements upon instabilities. For example, the MRE composite can be brought mechanically to the verge of wrinkling, and then be triggered with the application of a small-amplitude magnetic field. The reversibility and non-contact activation of the MRE buckling present new opportunities to reconfigure the underlying material architecture, which could be leveraged for load sensing, tunable energy absorption, and mechanical wave attenuation. Additionally, these magnetic tuning mechanisms could be used for applications such as controlling mechanical wave propagation [57], actuation of soft robotics [58], or adaptive metamaterials [59]. These findings demonstrate the promise of pairing magneto-mechanical coupling and mechanical instabilities in material systems for quick and remote actuation, and motivate further study into strategies to maximize this tuning effect.

#### Declaration of competing interest

The authors declare that they have no known competing financial interests or personal relationships that could have appeared to influence the work reported in this paper.

#### Data availability

Data will be made available on request.

#### Acknowledgements

The support of the Air Force Office of Scientific Research of the Air Force Research Laboratory under Grant #17RXCOR435 is acknowledged. SR thanks for the support of the European Research Council (ERC) through Grant No. 852281- MAGIC

#### Appendix A. Supplementary data

Supplementary data to this article can be found online at <https://doi.org/10.1016/j.compositesb.2022.110472>.

#### References

- [1] Forterre Y, Skotheim JM, Dumals J, Mahadevan L. How the venus flytrap snaps. *Nature* 2005;433:421–5.
- [2] Noblin X, Rojas N, Westbrook J, Llorens C, Argentina M, Dumais J. The fern sporangium: a unique catapult. *Science* 2012;335:1322.
- [3] Crosby AJ. Editorial: why should we care about buckling? *Soft Matter* 2010;6: 5660.



- [4] Su Y, Wu J, Fan Z, Hwang K-C, Song J, Huang Y, Rogers JA. Postbuckling analysis and its application to stretchable electronics. *J Mech Phys Solid* 2012;60:487–508.
- [5] Shan S, Kang S, Raney J, Wang P, Fang L, Candido F, Lewis J, Bertoldi K. Multistable architected materials for trapping elastic strain energy. *Adv Mater* 2015;27:4296–301.
- [6] Treml B, Gillman A, Buskohl P, Vaia R. Origami mechanologic. *Proc Natl Acad Sci USA* 2018;115:6916–21.
- [7] Jiang Y, Korpas L, Raney J. Bifurcation-based embodied logic and autonomous actuation. *Nat Commun* 2019;10:128. <https://www.nature.com/articles/s41467-018-08055-3>.
- [8] El Helou C, Buskohl PR, Tabor CE, Harne RL. Digital logic gates in soft, conductive mechanical metamaterials. *Nat Commun* 2021;12:1633. <https://www.nature.com/articles/s41467-021-21920-y>.
- [9] Truby R, Katschmann R, Lewis J, Rus D. Soft robotic fingers with embedded ionogel sensors and discrete actuation modes for somatosensitive manipulation. In: 2nd IEEE International Conference on Soft Robotics (RoboSoft); 2019. p. 322–9.
- [10] Jeong HY, An S-C, Seo IC, Lee E, Ha S, Kim N, et al. 3d printing of twisting and rotational bistable structures with tuning elements. *Sci Rep* 2019;9:1–9. <https://www.nature.com/articles/s41598-018-36936-6>.
- [11] Hu N, Burgueno R. Buckling-induced smart applications: recent advances and trends. *Smart Mater Struct* 2015;24:063001.
- [12] Bertoldi K, Gei M. Instabilities in multilayered soft dielectrics. *J Mech Phys Solid* 2011;59:18–42.
- [13] Rudykh S, DeBotton G. Stability of anisotropic electroactive polymers with application to layered media. *Zeitschrift für angewandte Mathematik und Physik* 2011;62:1131–42.
- [14] Rudykh S, Bhattacharya K, deBotton G. Multiscale instabilities in soft heterogeneous dielectric elastomers. *Proc R Soc A: Math Phys Eng Sci* 2014;470:20130618.
- [15] Goshkoderia A, Chen V, Li J, Juhl A, Buskohl P, Rudykh S. Instability-induced pattern formations in soft magnetoactive composites. *Phys Rev Lett* 2020;124:158002. <https://journals.aps.org/prl/abstract/10.1103/PhysRevLett.124.158002>.
- [16] Danas K, Triantafyllidis N. Instability of a magnetoelastic layer resting on a non-magnetic substrate. *J Mech Phys Solid* 2014;69:67–83.
- [17] Nam TH, Petrikova I, Marvalova B. Experimental characterization and viscoelastic modeling of isotropic and anisotropic magnetorheological elastomers. *Polym Test* 2020;81:106272.
- [18] Walter B, Pelteret J-P, Kashta J, Schubert D, Steinmann P. Preparation of magnetorheological elastomers and their slip-free characterization by means of parallel-plate rotational rheometry. *Smart Mater Struct* 2017;26:085004. <https://iopscience.iop.org/article/10.1088/1361-665X/aa6b63>.
- [19] Chen L, Gong X, Li W. Microstructures and viscoelastic properties of anisotropic magnetorheological elastomers. *Smart Mater Struct* 2007;16:2645–50.
- [20] Asadi Khanouki M, Sedaghati R, Hemmatian M. Experimental characterization and microscale modeling of isotropic and anisotropic magnetorheological elastomers. *Compos B Eng* 2019;176:107311.
- [21] Morillas JR, De Vicente J. Magnetorheology: a review. *Soft Matter* 2020;16:9614–42.
- [22] Li R, Sun L. Dynamic viscoelastic modeling of magnetorheological elastomers. *Acta Mech* 2014;225:1347–59.
- [23] Bastola AK, Hossain M. A review on magneto-mechanical characterizations of magnetorheological elastomers. *Compos B Eng* 2020;200:108348.
- [24] Garcia-Gonzalez D, Hossain M. A microstructural-based approach to model magneto-viscoelastic materials at finite strains. *Int J Solid Struct* 2021;208:119–32.
- [25] Saxena P, Hossain M, Steinmann P. A theory of finite deformation magneto-viscoelasticity. *Int J Solid Struct* 2013;50:3886–97.
- [26] Tiersten H. Coupled magnetomechanical equations for magnetically saturated insulators. *J Math Phys* 1964;5:1298–318.
- [27] Gorodkin S, James R, Kordonski W. Magnetic properties of carbonyl iron particles in magnetorheological fluids. *J Phys Conf* 2009;149:012051.
- [28] Keip M-A, Rambausek M. Computational and analytical investigations of shape effects in the experimental characterization of magnetorheological elastomers. *Int J Solid Struct* 2017;121:1–20.
- [29] Javili A, Chatzigeorgiou G, Steinmann P. Computational homogenization in magneto-mechanics. *Int J Solid Struct* 2013;50:4197–216.
- [30] Keip M-A, Rambausek M. A multiscale approach to the computational characterization of magnetorheological elastomers. *Int J Numer Methods Eng* 2016;107:338–60.
- [31] Castaneda PP, Galipeau E. Homogenization-based constitutive models for magnetorheological elastomers at finite strain. *J Mech Phys Solid* 2011;59:194–215. <https://www.sciencedirect.com/science/article/pii/S0022509610002383>.
- [32] Kadapa C, Hossain M. A unified numerical approach for soft to hard magneto-viscoelastically coupled polymers. *Mech Mater* 2022;166:104207.
- [33] Ivaneyko D, Toshchevikov V, Saphiannikova M, Heinrich G. Mechanical properties of magneto-sensitive elastomers: unification of the continuum-mechanics and microscopic theoretical approaches. *Soft Matter* 2014;10:2213–25.
- [34] Itskov M, Khiem VN. A polyconvex anisotropic free energy function for electro-and magnetorheological elastomers. *Math Mech Solid* 2016;21:1126–37.
- [35] Ciambella J, Favata A, Tomassetti G. A nonlinear theory for fibre reinforced magneto-elastic rods. *Proc R Soc A: Math Phys Eng Sci* 2018;474:20170703.
- [36] Ortigosa R, Gil AJ. A new framework for large strain electromechanics based on convex multi-variable strain energies: conservation laws, hyperbolicity and extension to electro-magneto-mechanics. *Comput Methods Appl Mech Eng* 2016;309:202–42.
- [37] Moon F, Pao Y-H. Magnetoelastic buckling of a thin plate. *Transactions of the ASME. Series E, Journal of Applied Mechanics* 1968;35:53–8.
- [38] Kankanala S, Triantafyllidis N. Magnetoelastic buckling of a rectangular block in plane strain. *J Mech Phys Solid* 2008;56:1147–69.
- [39] Dorfmann A, Ogden R. Nonlinear magnetoelastic deformations. *Q J Mech Appl Math* 2004;57:599–622.
- [40] Ottenio M, Destrade M, Ogden R. Incremental magnetoelastic deformations, with application to surface instability. *J Elasticity* 2008;90:19–42.
- [41] Psarra E, Bodelot L, Danas K. Two-field surface pattern control via marginally stable magnetorheological elastomers. *Soft Matter* 2017;13:6576–84.
- [42] Psarra E, Bodelot L, Danas K. Wrinkling to crinkling transitions and curvature localization in a magnetoelastic film bonded to a non-magnetic substrate. *J Mech Phys Solid* 2019;133:370–88. <https://www.sciencedirect.com/science/article/pii/S0022509619306179>.
- [43] Rudykh S, Bertoldi K. Stability of anisotropic magnetorheological elastomers in finite deformations: a micromechanical approach. *J Mech Phys Solid* 2013;61:949–67.
- [44] Goshkoderia A, Rudykh S. Stability of magnetoactive composites with periodic microstructures undergoing finite strains in the presence of a magnetic field. *Compos B Eng* 2017;128:19–29.
- [45] Pathak P, Arora N, Rudykh S. Magnetoelastic instabilities in soft laminates with ferromagnetic hyperelastic phases. *Int J Mech Sci* 2022;213:106862.
- [46] Hafeez MA, Usman M, Umer MA, Hanif A. Recent progress in isotropic magnetorheological elastomers and their properties: a review. *Polymers* 2020;12:1–35. <https://www.mdpi.com/2073-4360/12/12/3023>.
- [47] Jang D-D, Usman M, Sung S-H, Moon Y-J, Jung H-J. Feasibility study of MR elastomer-based base isolation system. *Journal of the Computational Structural Engineering Institute of Korea* 2008;21:597–605.
- [48] Komatsuzaki T, Inoue T, Terashima O. Broadband vibration control of a structure by using a magnetorheological elastomer-based tuned dynamic absorber. *Mechatronics* 2016;40:128–36.
- [49] Pierce C, Willey C, Chen V, Hardin J, Berrigan J, Juhl A, Matlack K. Adaptive elastic metastructures from magneto-active elastomers. *Smart Mater Struct* 2020;29:065004.
- [50] Zhang Q, Rudykh S. Magneto-deformation and transverse elastic waves in hard-magnetic soft laminates. *Mech Mater* 2022;169:104325.
- [51] Karami Mohammadi N, Galich PI, Krushynska AO, Rudykh S. Soft magnetoactive laminates: large deformations, transverse elastic waves and band gaps tunability by a magnetic field. *J Appl Mech* 2019;86:111001. <https://asmedigitalcollection.asme.org/appliedmechanics/article/86/11/111001/958388/Soft-Magnetoactive-Laminates-Large-Deformations>.
- [52] Yu K, Fang NX, Huang G, Wang Q. Magnetoactive acoustic metamaterials. *Adv Mater* 2018;30:1706348.
- [53] Willey C, Chen V, Scalzi K, Buskohl P, Juhl A. A reconfigurable magnetorheological elastomer acoustic metamaterial. *Appl Phys Lett* 2020;117:104102.
- [54] Hooshiar A, Payami A, Dargahi J, Najarian S. Magnetostriction-based force feedback for robot-assisted cardiovascular surgery using smart magnetorheological elastomers. *Mech Syst Signal Process* 2021;161:107918.
- [55] Dorm C, Bodelot L, Danas K. Experiments and numerical implementation of a boundary value problem involving a magnetorheological elastomer layer subjected to a non-uniform magnetic field. *J Appl Mech, Transactions ASME* 2021;88:071004. <https://asmedigitalcollection.asme.org/appliedmechanics/article/88/7/071004/1104292/Experiments-and-Numerical-Implementation-of-a>.
- [56] Li Y, Kaynia N, Rudykh S, Boyce MC. Wrinkling of interfacial layers in stratified composites. *Adv Eng Mater* 2013;15:921–6. <https://onlinelibrary.wiley.com/doi/10.1002/adem.201200387>.
- [57] Rudykh S, Boyce M. Transforming wave propagation in layered media via instability-induced interfacial wrinkling. *Phys Rev Lett* 2014;112:034301.
- [58] Hines L, Petersen K, Lum GZ, Sitti M. Soft actuators for small-scale robotics. *Adv Mater* 2017;29:1603483.
- [59] Harne R, Deng Z, Dapino M. Adaptive magnetoelastic metamaterials: a new class of magnetorheological elastomers. *J Intell Mater Syst Struct* 2018;29:265–78.